



Fluctuation-induced transport and poloidal rotation in the interchangeable module stellarator

P. G. Matthews, D. T. Anderson, F. S. B. Anderson, J. L. Shohet, and J. N. Talmadge

Citation: [Physics of Fluids B](#) **5**, 4061 (1993); doi: 10.1063/1.860574

View online: <http://dx.doi.org/10.1063/1.860574>

View Table of Contents: <http://scitation.aip.org/content/aip/journal/pofb/5/11?ver=pdfcov>

Published by the [AIP Publishing](#)

Articles you may be interested in

[Poloidal rotation in tokamaks with large electric field gradients](#)

[Phys. Plasmas](#) **2**, 159 (1995); 10.1063/1.871105

[Comment on "Effects of neutral beam injection on poloidal rotation and energy transport in tokamaks"](#)
[[Phys. Fluids B](#) **5**, 3012 (1993)]

[Phys. Fluids B](#) **5**, 4505 (1993); 10.1063/1.860568

[Effects of neutral beam injection on poloidal rotation and energy transport in tokamaks](#)

[Phys. Fluids B](#) **5**, 3012 (1993); 10.1063/1.860687

[Effect of a poloidal shear flow on the probability of accessing the multiple saturated states in the resistive interchange instability](#)

[Phys. Fluids B](#) **5**, 1795 (1993); 10.1063/1.860815

[Ion orbit loss and poloidal plasma rotation in tokamaks](#)

[Phys. Fluids B](#) **4**, 171 (1992); 10.1063/1.860430

Fluctuation-induced transport and poloidal rotation in the interchangeable module stellarator

P. G. Matthews, D. T. Anderson, F. S. B. Anderson, J. L. Shohet, and J. N. Talmadge
Torsatron/Stellarator Laboratory, University of Wisconsin-Madison, Madison, Wisconsin 53706

(Received 7 June 1993; accepted 3 August 1993)

Probe measurements over the two-dimensional plasma cross section of the average and fluctuating density, electron temperature, and potential, as well as the Reynolds stress, have been made in the Interchangeable Module Stellarator (IMS) [D. T. Anderson, J. A. Derr, and J. L. Shohet, *IEEE Trans. Plasma Sci.* **PS-9**, 212 (1981)]. These measurements were performed at two magnetic field strengths, and also when a positively biased electrode induces a poloidal plasma flow. The data shows the fluctuation-induced transport to be poloidally asymmetric and dependent upon the location of the electron cyclotron resonance position, and upon the electrode biasing. The induced poloidal plasma flow changes the nominally outward fluctuation-induced particle transport to be inward (negative radial transport) by changing the phase relationship of the density and potential oscillations. The amplitude of the density and potential fluctuations are, in general, not reduced by the sheared poloidal flow. Calculations are presented comparing the computed Reynolds stress induced poloidal plasma flows with the flow calculated from momentum balance.

I. INTRODUCTION

Neoclassical transport does not adequately predict the gross particle and energy confinement observed on present toroidal devices, and broadband plasma turbulence has been suggested to be the cause of the anomalous transport.^{1,2} Recent investigations of the effects of electrostatic plasma fluctuations on the transport processes in toroidal systems have been performed on tokamaks,³⁻⁵ stellarators,⁶ and reversed-field pinches⁷ (RFP). In such studies measurements of the local fluctuation-induced transport were made at relatively few spatial locations in the edge plasma regions. Estimates of the total fluctuation-induced particle and energy losses thereby require the assumption of poloidal and toroidal symmetry. In order to investigate the assumption of poloidal symmetry of the fluctuations and the fluctuation-induced transport, in this work we describe detailed measurements of the fluctuating density, plasma potential, electron temperature, the calculated electrostatic fluctuation-induced particle transport ($\langle \tilde{n}_e \tilde{v}_r \rangle$), and Reynolds stress ($\langle \tilde{v}_r \tilde{\rho}_\theta \rangle$) over the entire two-dimensional plasma cross section.

Sheared poloidal rotation has been suggested as a mechanism to suppress plasma turbulence⁸ and reduce the anomalous transport. Strongly sheared poloidal plasma flows are induced in the Interchangeable Module Stellarator⁹ (IMS) by means of a positively biased electrode placed in the plasma edge, similar to techniques used in the Tokamak Experiment for Technically Oriented Research¹⁰ (TEXTOR) and the Continuous Current Tokamak¹¹ (CCT). The effect of these flows on the transport is observed to alter the magnitude and direction of the radial flux in IMS, but not substantially reduce the fluctuation levels.

In addition, IMS exhibits a factor of 2 change in particle confinement time, depending upon the location of the

electron cyclotron heating (ECH) resonance zone. The complete two-dimensional fluctuation measurements were performed for each of these "good" and "bad" particle confinement configurations to determine the role of the plasma fluctuations on the particle confinement time. It is concluded that the fluctuation-induced transport is the dominant particle loss mechanism in the "bad" confinement configuration, while it is not a significant loss mechanism in the "good" configuration.

Finally, it has also been suggested that fluctuations in the radial and poloidal velocity components can couple to generate poloidal flow through the Reynolds stress, and that such a mechanism might be involved in the low (L) to high (H) mode confinement transition observed in tokamaks.¹² The multipoint emissive probe measurements used in this study allow the calculation of the simultaneous fluctuating electric field components necessary to compute the Reynolds stress. The Reynolds stress-driven poloidal flow is then estimated from these calculations and measurements of the poloidal damping time. While it is found to be comparable in magnitude to the equilibrium flows in nonbiased IMS discharges, the errors associated with this measurement, and the absence of an independent measurement of the poloidal flow, make the existence of the Reynolds stress-driven flow difficult to determine.

This paper is organized as follows. In Sec. II we describe the experimental apparatus and measurement techniques used to obtain the plasma parameters and for computation of the fluctuation-induced transport. In Sec. III we describe the impact of the electrode bias, and positioning of the ECH resonance on (a) the steady-state parameters, (b) the observed fluctuation levels, (c) the fluctuation-induced particle transport, and (d) the Reynolds stress-driven poloidal flows. The results for the four experimental configurations (two magnetic field strengths, both with and without electrode bias) are presented simul-

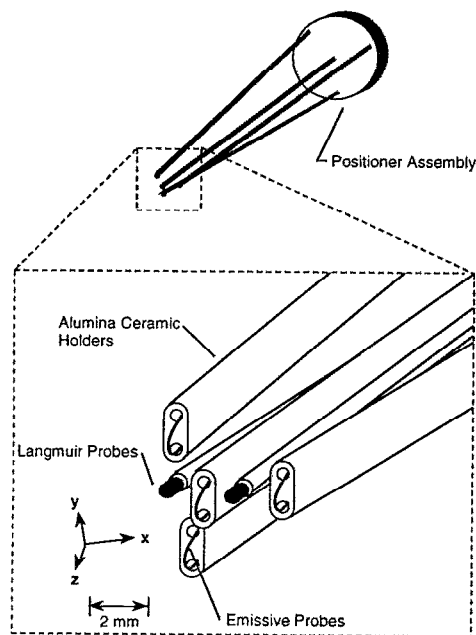


FIG. 1. Langmuir/emissive probe array used for measuring plasma fluctuations.

taneously throughout this work so that their common features, or differences, can be more easily compared. Finally, in Sec. IV we provide a summary of the major results.

II. EXPERIMENTAL SETUP AND ANALYSIS

IMS is a seven field period, $L=3$ modular stellarator ($R=0.4$ m, $\bar{a}=0.04$ m, $\iota_0=0.0$, $\iota_a=0.6$) with typical ECH discharge parameters; $\bar{n}_e=5\text{--}11 \times 10^{10} \text{ cm}^{-3}$, $T_e=4\text{--}10$ eV, $T_i=1\text{--}3$ eV, $B_0=0.24$ and 0.26 T, $P_{\text{ECH}}=1$ kW at $f=7.275$ GHz, and pulse length of 10 msec. Particle confinement times are estimated by measuring the plasma efflux onto the divertor strike plates.¹³ Discharges performed at the central magnetic field strength of 0.26 T, corresponding to the ECH resonance zone located on the magnetic axis, have a typical particle confinement time of 0.4 msec, while at $B_0=0.24$ T, the resonance zone is concentrated on the inboard side of the torus, and the confinement time increases to 0.8 msec. Midway through the ECH pulse, an electrode placed 1 cm inside the separatrix is biased to +80 V, which creates a strong positive radial electric field (1–4 kV/m) and drives a large poloidal rotation of the edge plasma (5–15 km/sec).

Measurements of the plasma density, plasma potential, electron temperature, and fluctuations in these quantities were made over the entire cross section of the plasma using an array of two Langmuir and four emissive probes, as shown in Fig. 1. The emissive probes consist of small filament loops (<0.6 mm across) of 0.0254 mm diam tungsten wire heated by a direct current into thermal electron emission, and are used to measure the plasma potential, $\Phi_p(t)$ directly. The proper level of emission was determined experimentally using the inflection point method,¹⁴ after which the probes are allowed to float, so as to follow

the potential oscillations within the plasma. The probes are separated by ≈ 2 mm, and their spatial arrangement allows the local determination of $-\nabla\Phi_p(r,t)$ in three dimensions. The two Langmuir probes were used to measure the plasma floating potential, $\Phi_f(t)$, and ion saturation current, $I_{\text{sat}}(t)$. Electron temperature and plasma density were then determined using the relations

$$T_e(t) = \frac{\Phi_p(t) - \Phi_f(t)}{\alpha} \quad \text{and} \quad n(t) = \frac{I_{\text{sat}}(t)}{0.8qA} \sqrt{\frac{m_i}{T_e(t)}}, \quad (1)$$

where $\alpha=1.7$ is an experimentally determined constant (usual theoretical estimates of α are $\approx 2\text{--}3.3$ ^{7,17}), q is the ionic charge, A is the effective surface area of the probe, and m_i is the ion mass. The constant α was determined by first measuring T_e with a swept Langmuir probe and then dividing T_e into the difference of the average values of $\Phi_p(t)$ and $\Phi_f(t)$. Radial profiles of ion temperatures were measured using the gridded energy analyzer (GEA) technique.^{15,16} For the discharges used in this work, the ion temperature profile was found to be flat with a temperature of 2.1 ± 0.2 eV.

The physical spacing and size of the probes tips shown in Fig. 1 was determined using the following criterion: the probes must be large enough to adequately measure the parameters of interest, their separation should be large enough to ensure that they do not influence each other, and their separation must be small enough to fit within the correlation distance of the density and potential fluctuations. The criteria for the probe tip size is that the probe radius should be large compared to the electron gyroradius (0.023 mm) and Debye length (0.06 mm) and smaller than the ion gyroradius (0.8 mm).¹⁷ The two Langmuir probes have an effective radius of 0.25 mm. The emissive probe's filament forms a loop ≈ 0.6 mm in diameter, but the effective radius was determined to be ≈ 0.2 mm by biasing an emissive probe into ion saturation and equating the measured current to that of the Langmuir probe of which the surface area is known. Thus, each of these probes satisfy the criteria for probe tip size.

The fluctuation correlation length was measured by calculating the correlation coefficient of the density fluctuations as a function of the distance between two Langmuir probes. The $1/e$ point of the correlation coefficient was determined at $\approx 3\text{--}4$ mm. Thus, the approximate 2 mm spacing between probes was used to ensure the probes were spaced within this distance, and the orientation of the probes was optimized with respect to the magnetic field direction to minimize possible shadowing effects. Even though the probes were many Debye lengths apart (≈ 15 Debye lengths at the lowest plasma density) and five out of the six probes in the array are floating (drawing almost no current from the plasma), experimental studies were performed to determine if this spacing would cause the probes to influence each other. These studies consisted of monitoring the density, plasma potential, and their frequency spectra on one or two of the probes in various scenarios of electron emission, applied ion-saturation bias, probe presence, and probe array orientations within the plasma. In all scenarios, the measured parameters, and their fluctuation

spectral characteristics, showed no influence from the other probes, as the plasma effectively isolated all the probe tips. It is important to note that these probe tips are separated by 2.4 ion gyroradii, and as a consequence, these probes are sampling adjacent plasma volumes (magnetic flux tubes), which may result in nonindependent measurements of density and potential. This condition may influence the calculation of the fluctuation-induced transport, possibly causing an underestimate of the flux. However, the experiments investigating the probe to probe isolation indicate that these probes are sampling independent plasma volumes.

The only perturbation caused by the probe array was to lower the overall plasma density by $\approx 5\%$, as measured by a microwave interferometer, when the array was inserted far into the plasma, where there is the most obstruction caused by the alumina ceramic holders (see Fig. 1). This effect on the measured density by the Langmuir probe was compensated by normalizing the average density to that measured by the interferometer.

The signals used for the calculation of the fluctuation-induced transport and Reynolds stress were selected to avoid transients associated with the initial neutral hydrogen gas breakdown, and the poloidal plasma spin-up/spin-down phases of the electrode biasing. This selection provided two 3.5 msec time slices when the plasma was in equilibrium. For statistical purposes, these intervals were further subdivided into records ≈ 0.6 msec in length, or about 300 samples at a digitization rate of 500 kHz. The local radial electrostatic fluctuation-induced particle flux was computed using $\Gamma_r = \langle \tilde{n}_e \tilde{v}_r \rangle$, where $\langle \rangle$ indicates an ensemble average.¹⁸ The fluctuating radial velocity \tilde{v}_r is determined from the fluctuating $\tilde{\mathbf{E}} \times \mathbf{B}$ drift, where \tilde{E} is determined from the four emissive probes. The electrostatic fluctuation-induced transport can be written in spectral form as¹⁸

$$\Gamma_r = \langle \tilde{n}_e \tilde{v}_r \rangle = \frac{C_{nE}(0)}{B} = \frac{2}{B} \int_0^\infty d\omega k_p(\omega) \gamma_{n\phi}(\omega) \times \sin[\alpha_{n\phi}(\omega)] \sqrt{P_{nn}(\omega) P_{\phi\phi}(\omega)}, \quad (2)$$

where $C_{nE}(0)$ is the cross-correlation function at $\tau=0$, $k_p(\omega)$ is the experimentally measured dispersion relation of poloidal potential fluctuations that is obtained by computing the phase difference between adjacent emissive probes and dividing by their poloidal separation, $\gamma_{n\phi}(\omega)$ is the amplitude coherence between density and potential, $\alpha_{n\phi}(\omega)$ is the phase angle between the density and potential fluctuations, and $P_{nn}(\omega)$ and $P_{\phi\phi}(\omega)$ are the amplitude spectra of the density and potential fluctuations, respectively.

The surface-averaged Reynolds stress-driven poloidal flow V_θ is estimated by¹²

$$V_\theta = \gamma \left(\frac{\partial \langle \tilde{v}_r \tilde{v}_\theta \rangle}{\partial r} \right), \quad (3)$$

where γ is the poloidal damping time, and the parentheses $\langle \rangle$ indicate an average over the magnetic flux surface. The poloidal fluctuating velocity \tilde{v}_θ was determined in the same manner as \tilde{v}_r . A poloidal damping time of 20–30 μsec was determined from the measured decay of the poloidal plasma flow after the electrode bias was turned off.¹⁹ This damping time has been shown to be relatively constant in the center regions of the IMS plasma due to collisions with neutrals and increasing in the edge plasma region, where viscosity effects become significant.²⁰ The equilibrium poloidal flow velocity is computed from the momentum balance equation,

$$V_\theta = \frac{\nabla P_i}{enB} - \frac{E}{B}, \quad (4)$$

where ∇P_i is the radial gradient of the ion pressure, e is the electron charge, n is the measured plasma density profile, B is the magnetic field strength, and E is the radial electric field computed from the measured potential distribution. The ion pressure is determined from the measured radial density profile and measured ion temperature (2.1 eV) using $P_i = nkT_i$, where k is Boltzmann's constant. The ion pressure gradient is then determined from this profile.

III. OBSERVATIONS AND DISCUSSION

A. Steady-state parameters

The radial profiles of plasma density, electron temperature, and potential for the four experimental configurations are presented in Figs. 2 and 3. The three profiles in Fig. 2 correspond to the on-axis magnetic field strength of 0.24 T (ECH on inboard side), while the three in Fig. 3 are for 0.26 T on axis (central ECH). The impact of the electrode biasing on these profiles is shown by the dashed lines. The standard case (no electrode bias) is shown by the solid lines. The radial profiles result from averaging the measured parameters found within the poloidal cross section that are on the magnetic flux surfaces. The location of these surfaces are determined from vacuum flux surface mapping using an electron gun and a fluorescent screen.²¹ The average radius of the flux surface, normalized to the average radius of the separatrix, is used as the abscissa, and the profiles were computed using extrapolated magnetic flux surfaces beyond the separatrix to examine the first few millimeters of the ergodic region. For all profiles, the physical position of the biasing electrode is at $r/a=0.8$.

The profiles of Figs. 2(a) and 3(a) show that there is approximately twice the density at $B_0=0.24$ T operation over that at $B_0=0.26$ T. The factor of 2 difference in particle confinement time is a result of a twofold increase in density between the two fields, since the total particle loss rate, as measured by the current to the divertor strike plates, remains about the same for each field configuration. The density obtained at 0.24 T has a less hollow profile than at 0.26 T. For both magnetic field strengths, the electrode biasing causes the peak in the profile to become shifted inward in minor radius, and significantly changes the edge gradients. For the 0.24 T case, the local density increases by $\approx 35\%$ for $r/a < 0.6$, which is not observed for

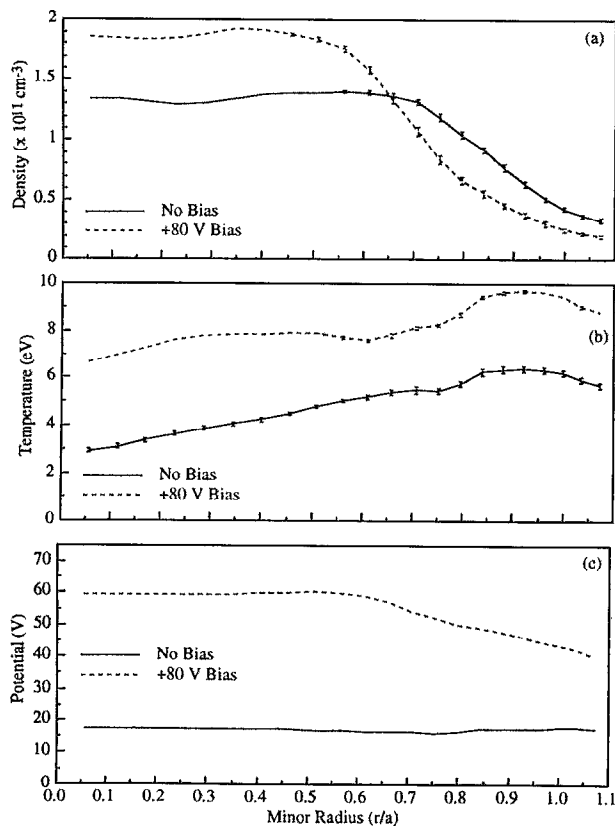


FIG. 2. Radial profiles of (a) plasma density, (b) electron temperature, and (c) plasma potential, at 0.24 T central magnetic field strength, with and without electrode biasing.

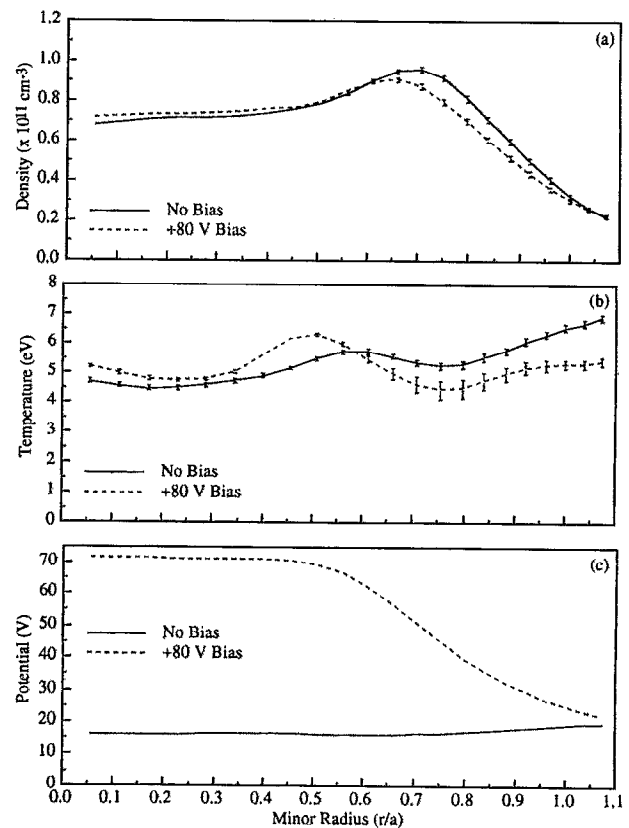


FIG. 3. Radial profiles of (a) plasma density, (b) electron temperature, and (c) plasma potential, at 0.26 T central magnetic field strength, with and without electrode biasing.

0.26 T field operation. The local density is seen to decrease in the vicinity of the biased electrode ($r/a=0.8$). The changes in profile shape, as a result of the electrode bias, changes the line-average density only minimally over that of the nonbiased case ($\approx 8.7\%$ increase for 0.24 T and $\approx 2.5\%$ decrease for 0.26 T).

The radial profiles of electron temperature are seen, in Figs. 2(b) and 3(b), to be more hollow in the 0.24 T case than for 0.26 T. The electrode bias causes a significant increase in temperature (50%, or ≈ 3 eV) at the 0.24 T field, while less significant alterations occur at the 0.26 T field. The same +80 V electrode bias also affects the plasma potential profiles differently for the two magnetic fields [Figs. 2(c) and 3(c)]. A higher peak radial electric field is generated for the 0.26 T case (3.5 kV/m) than for the 0.24 T case (1.2 kV/m). In addition, the plasma potential only reaches a value of +60 V (with respect to the vacuum vessel) in the center of the IMS plasma for 0.24 T operation, as opposed to +72 V in the 0.26 T case. In either case, the radial electric field is dramatically increased over that in the standard discharges.

Two examples of the two-dimensional distribution of the steady-state plasma parameters are shown in Figs. 4 and 5 for the plasma density in the 0.24 T, no bias configuration, and the potential in the 0.26 T, +80 V biased electrode configuration, respectively. The dashed contours on these plots show the location of the magnetic flux sur-

faces. There is a small region in the lower portion of these graphs where probe measurements were not possible due to access constraints. This region was excluded in the calculation of parameter averages on a magnetic flux surface.

The density contours of Fig. 4 show good alignment with the vacuum magnetic flux surfaces, particularly in the edge regions of the plasma. The potential contours in the biased 0.26 T configuration of Fig. 5 show excellent agreement with the magnetic flux surface which is typical of the

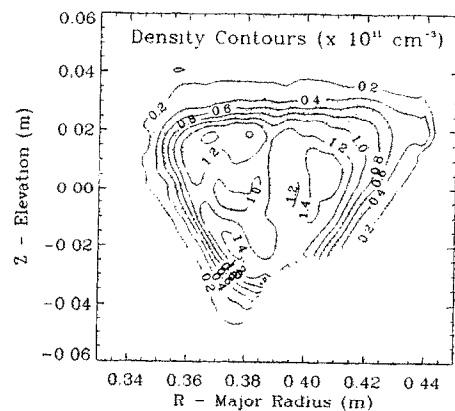


FIG. 4. Contour plot of plasma density in IMS at 0.24 T field operation with no electrode bias.

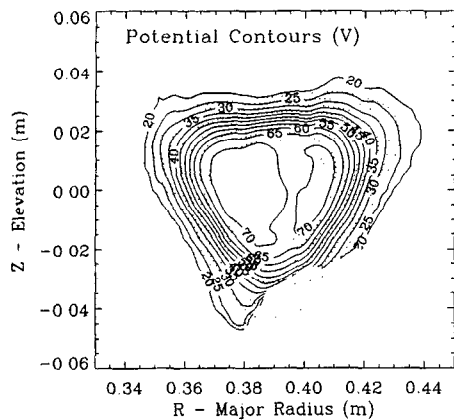


FIG. 5. Plasma potential contours with electrode biased to +80 V at 0.26 T field operation.

density and electron temperature distributions in the biased configuration of both magnetic field strengths.

B. Fluctuation levels

The normalized fluctuation amplitude levels for plasma density, electron temperature, and potential are comparable for unbiased plasmas at the two magnetic fields, but are affected differently by the application of the +80 V electrode bias. Figures 6(a) and 7(a) show the normalized density fluctuation amplitude averaged over the magnetic flux surfaces using the same procedures as for Figs. 2 and 3. For both figures, the density fluctuation levels are smaller in the interior of the plasma ($r/a < 0.6$), and significantly increase from this point to the plasma edge. These density fluctuation levels are comparable in magnitude, and in profile shape, to those seen in other devices.^{6,7,22} The electrode bias causes a 50% increase in density fluctuation levels for $r/a > 0.5$ at the 0.24 T operation while causing a lesser impact at the 0.26 T field.

The normalized electron temperature fluctuation levels [Figs. 6(b) and 7(b)] are smaller than the observed density fluctuation levels, but show the same trend of increasing toward the plasma edge. A 140% increase in temperature fluctuation occurs at $r/a \approx 0.8$ when the electrode is biased in the 0.26 T field, in contrast to the decrease seen throughout the minor radius for the 0.24 T case. The magnitude of the temperature fluctuations in IMS are somewhat less than the 0.25 levels reported in the Madison Symmetric Torus (MST) RFP edge plasma,⁷ where temperature oscillations were very important in the calculation of the associated electrostatic fluctuation-induced transport. The electron temperature fluctuations are included in the IMS calculation of the fluctuation-induced transport by including the instantaneous measurement of $T_e(r)$ in the calculation of the plasma density as given in Eq. (1).

The plasma potential fluctuation levels (normalized to the local steady-state value of electron temperature) are shown in Figs. 6(c) and 7(c). These levels are similar in magnitude as those for the electron temperature. There is a common trend in all the radial profiles of Figs. 6 and 7, in

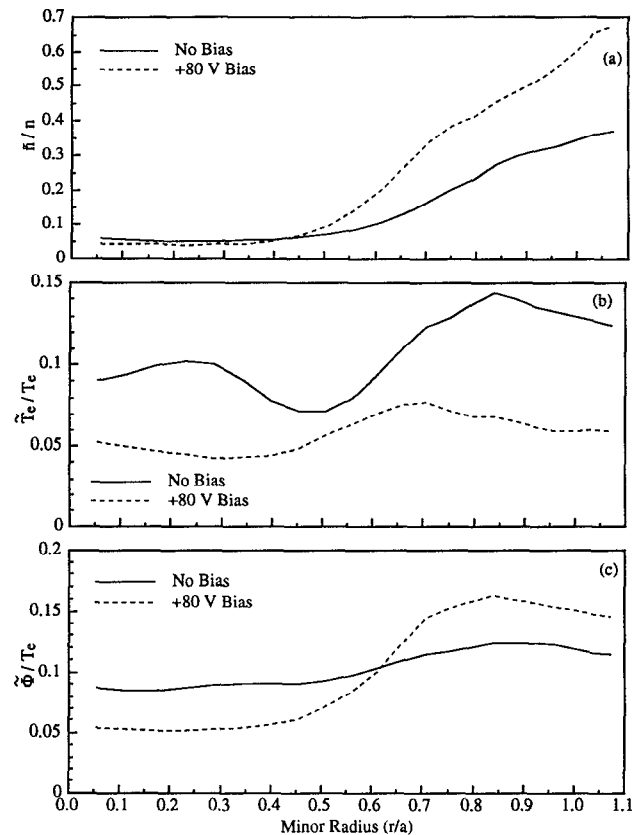


FIG. 6. Normalized fluctuation amplitude profiles for (a) plasma density, (b) electron temperature, and (c) plasma potential, at 0.24 T field operation, with and without electrode biasing.

that the fluctuation amplitudes begin to rise at a particular minor radius for each of the four experimental configurations. Many instabilities thought to be connected with plasma fluctuations are driven by gradients in the density and temperature, and in the pressure. The radial electron pressure profiles of Fig. 8(a) indicate a change in sign of the pressure gradient at $r/a \approx 0.65$, for the standard case, and $r/a \approx 0.45$ for the biased electrode case. These points correlate well with the radial position, where the fluctuation levels begin to increase in the standard and biased configurations, respectively. Similar agreement is found for the radial position of the sign change in the pressure gradient in the 0.26 T field case [Fig. 8(b)], with the corresponding increases in fluctuation levels. Gradients in the surface-average value of the magnetic field must also be considered because certain instabilities may be stabilized by "favorable" curvature, $\nabla B \cdot \nabla P < 0$.¹ The nominal IMS magnetic topology used for these experiments has a magnetic "hill" configuration throughout the entire minor radius. Thus, positive radial pressure gradients, found in the hollow section of IMS pressure profiles, attain "favorable" curvature, while the negative edge pressure gradients result in "unfavorable" curvature. These regions of favorable and unfavorable curvature, correlate well with the regions of low, and increasing fluctuation levels, respectively.

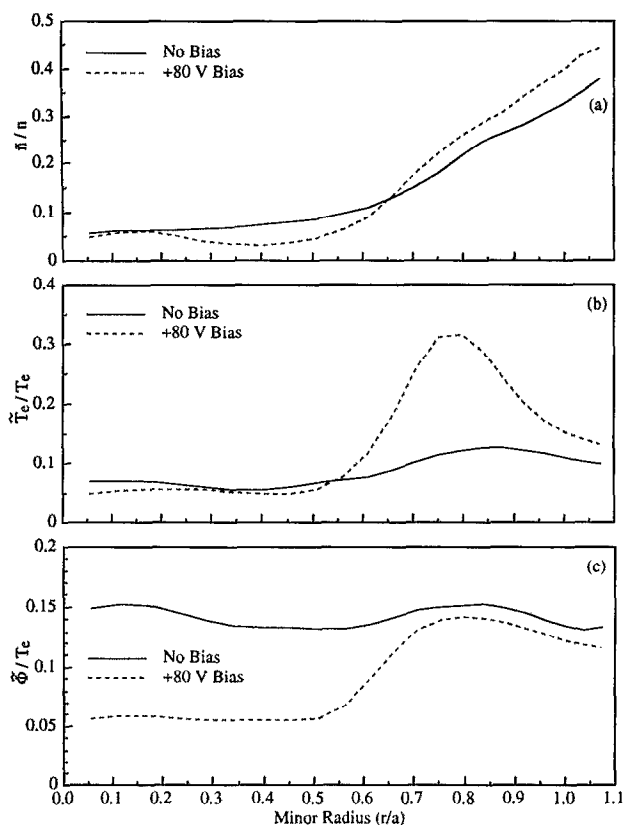


FIG. 7. Normalized fluctuation amplitude profiles for (a) plasma density, (b) electron temperature, and (c) plasma potential, at 0.26 T field operation with and without electrode biasing.

C. Fluctuation-induced transport

Using the formulation presented in Eq. (2), the density and potential fluctuations give rise to the radial fluctuation-induced transport shown in the two-

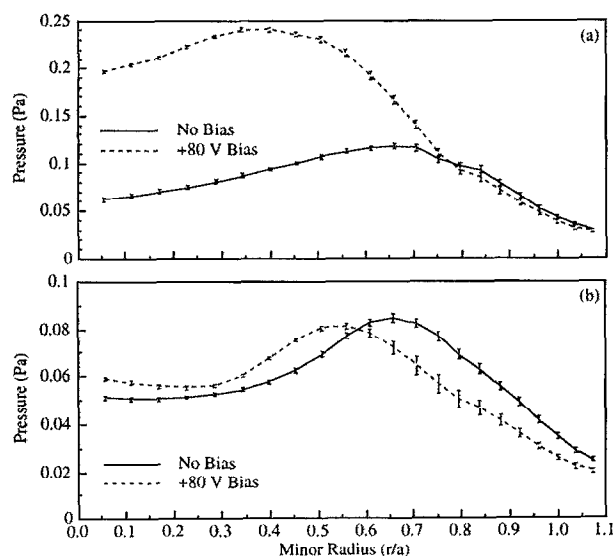


FIG. 8. Radial profiles of surfaced-averaged electron pressure for (a) 0.24 T magnetic field operation and (b) 0.26 T operation.

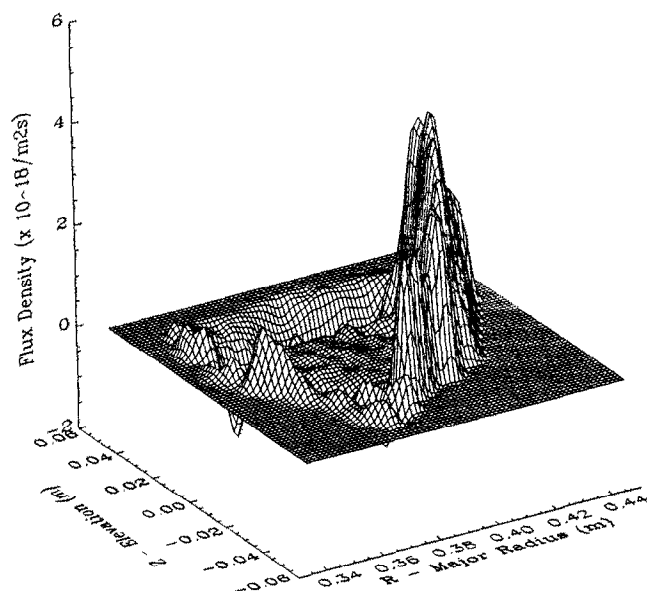


FIG. 9. Surface plot of radial fluctuation-induced transport in IMS for 0.24 T field, no electrode bias.

dimensional surface plots of Figs. 9–12 for the four experimental configurations. The transport is plotted on a square grid with respect to the major radius R and elevation Z .

From the figures, it can be seen that the particle flux is not symmetric on the flux surfaces. In the 0.24 T case (Fig. 9), the flux is predominantly located on the outside midplane of the device, while the 0.26 T case (Fig. 10) shows peaks in the flux on both the inside and outside midplanes. In contrast to the asymmetry observed in the particle flux in these regions, the steady-state density and potential are roughly constant on the flux surface. The transport is negligible in amplitude in the interior of the plasma, corre-

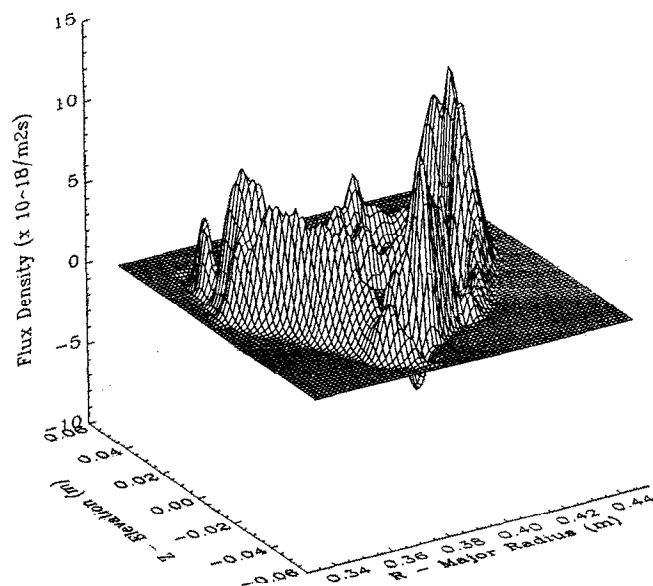


FIG. 10. Surface plot of radial fluctuation-induced transport in IMS for 0.26 T field, no electrode bias.

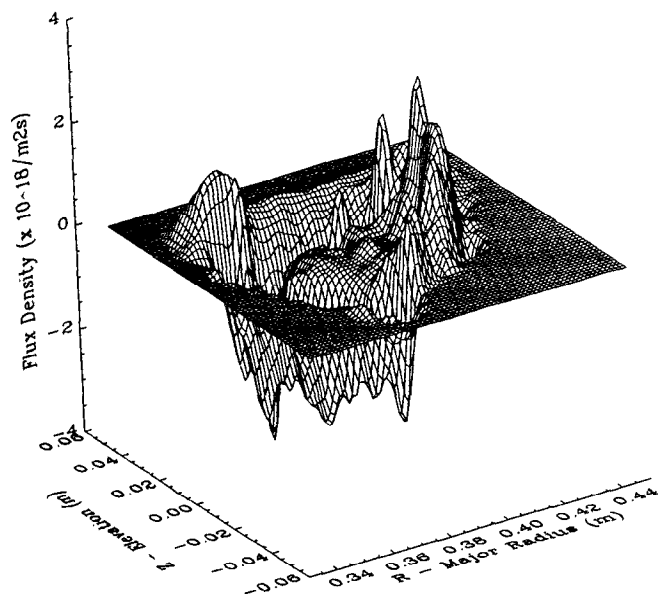


FIG. 11. Surface plot of radial fluctuation-induced transport in IMS for 0.24 T field, +80 V electrode bias.

sponding to where the density fluctuations were seen to be small [Figs. 6(a) and 7(a)]. Beyond this region, there are areas where the radial transport is negative, or inward, located at $r/a \approx 0.5$ on the inside midplane in the 0.26 T configuration. Beyond $r/a \approx 0.5$, the transport increases dramatically, which is consistent with the observed increase in the density, temperature, and potential fluctuation amplitudes at this radius.

The impact of electrode biasing on the radial fluctuation-induced transport is shown in Figs. 11 and 12. It can be seen from the figures that, compared to Figs. 9 and 10, the regions where the fluctuation-induced particle

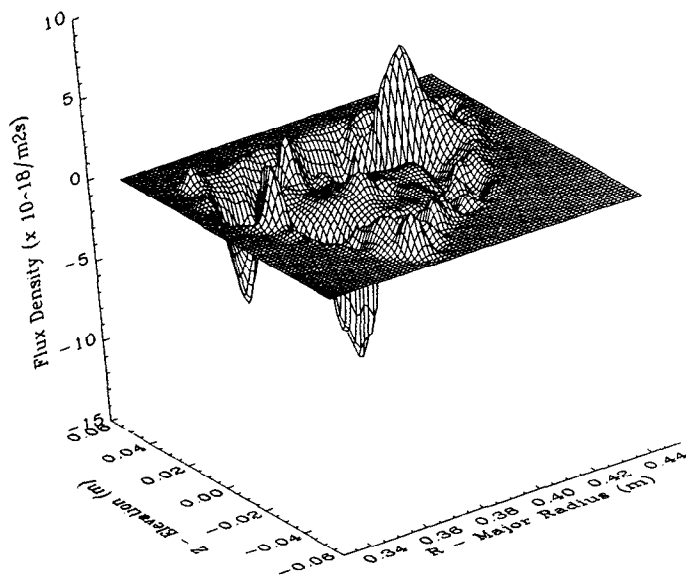


FIG. 12. Surface plot of radial fluctuation-induced transport in IMS for 0.26 T field, +80 V electrode bias.

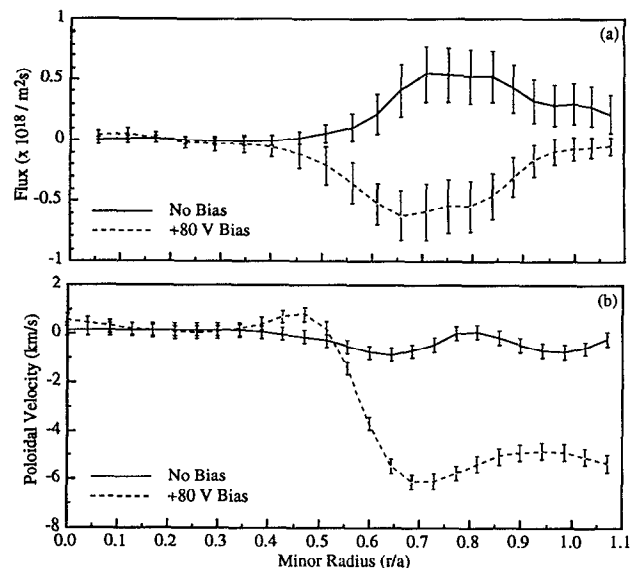


FIG. 13. Radial profiles of (a) average radial fluctuation-induced transport, and (b) poloidal rotation velocity at a 0.24 T field, with and without electrode biasing.

flux is negative have increased considerably due to the electrode biasing. Again, there are major poloidal asymmetries associated with the particle flux that do not correlate well with any asymmetries seen in the steady-state distributions of plasma density and potential. The largest asymmetries in the radial flux are located in the region $r/a > 0.5$, where there are large edge density and pressure gradients. The potential and density contours in this same radial region show the steady-state parameters are relatively uniform on the magnetic surfaces.

The net effect of the electrode biasing on the radial fluctuation-induced transport is evident in the surface-averaged particle flux profiles shown in Figs. 13(a) and 14(a). In each case, the particle flux has changed from mostly outward to mostly inward (negative flux) by the electrode biasing. An additional feature of the unbiased configuration profiles is that the peak in the outward transport for the 0.24 T field occurs at $r/a \approx 0.8$, while the transport in the 0.26 T field peaks out at the separatrix. This feature is inconsistent with the trend exhibited in the 0.26 T field, where the transport increases with increasing density fluctuation amplitude levels [Figs. 6(a) and 7(a)]. There is also a strong correlation between this inward flux and the induced poloidal rotation velocity, in that the maximum inward flux occurs at the peak of the rotation shown in Figs. 13(b) and 14(b) (dashed lines), where the induced poloidal rotation is in the ion diamagnetic drift direction.

Figures 13(a) and 14(a) also show that the level of the fluctuation transport for the nonbiased, 0.26 T field is much higher than when the resonance is placed on the inboard side of the torus. The total particle loss rate due to fluctuation-induced transport is computed by integrating the measured flux over the surface area of the plasma at the separatrix,

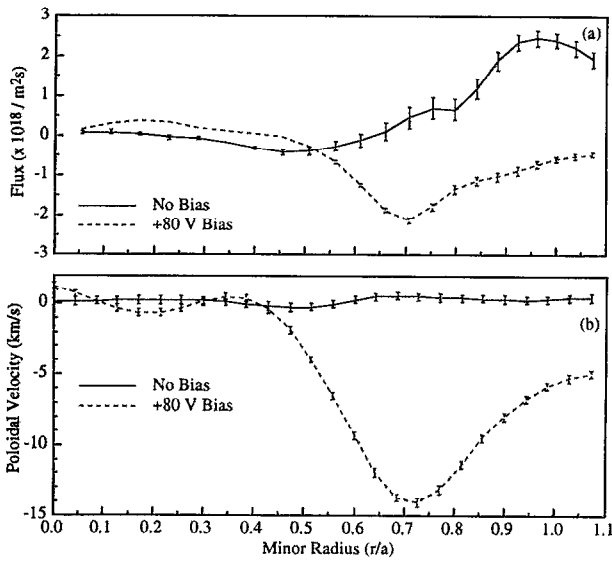


FIG. 14. Radial profiles of (a) average radial fluctuation-induced transport and (b) poloidal rotation velocity at a 0.26 T field, with and without electrode biasing.

$$\text{loss rate} = \int_0^{2\pi} d\phi \int_0^{2\pi} d\theta \Gamma(\theta) r(\theta) [R_0 + r(\theta) \cos \theta], \quad (5)$$

where ϕ and θ are the toroidal and poloidal angles, respectively, $\Gamma(\theta)$ is the measured particle flux at the separatrix obtained from Figs. 9 and 10, $r(\theta)$ is the minor radius of the separatrix measured from the magnetic axis of IMS, and R_0 is the major radius of the magnetic axis (0.388 m). This estimation assumes that there is toroidal symmetry for the observed particle flux, since the measured fluctuation-induced particle flux is a function of poloidal angle on the separatrix at one toroidal location. These losses can be compared to the total particle losses as measured by the IMS divertor strike plates, and show that when the particle confinement is better (0.24 T) the fluctuation transport accounts for $\approx 10\%$ of the total particle losses, while accounting for 87% of the losses for the 0.26 T field. This indicates that the increase in electrostatic fluctuation-induced transport is a major factor for the decreased particle confinement of the 0.26 T field configuration.

The components of Eq. (2) can be examined to show how the fluctuation-induced transport has been altered by the electrode bias. For this analysis, the components essential to the calculation of the transport are identified from Eq. (2), averaged over frequency, and over the magnetic flux surfaces, and plotted versus minor radius to show their general trends. Note that this analysis may not be an accurate representation of how the transport is affected at a specific point in the plasma. This analysis is intended only to show possible global trends for the fluctuation components and the calculation of the fluctuation-induced transport.

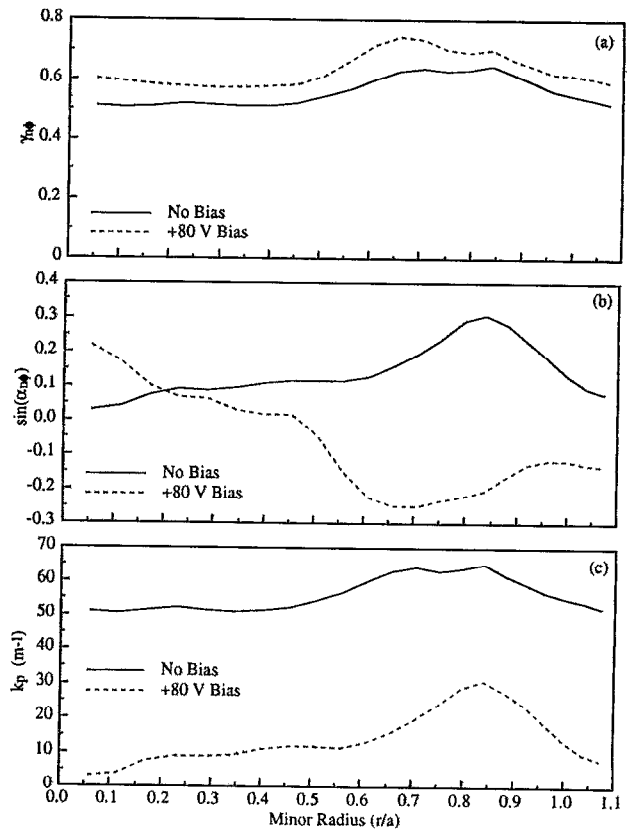


FIG. 15. Radial profiles of (a) average coherence, (b) phase angle relationship and (c) $k(\omega)$, for plasma density and potential fluctuations, showing the effects of electrode biasing at 0.24 T magnetic field operation.

The plasma density and potential fluctuation amplitudes of Figs. 6 and 7 are a measure of the components $P_{nn}(\omega)$ and $P_{\phi\phi}(\omega)$. The density fluctuation levels are seen to increase with the induced poloidal rotation, and the potential fluctuation amplitudes are still significant in the strong poloidal flow region. The radial profiles of the surfaced-averaged coherency are given in Figs. 15(a) and 16(a). The 0.26 T case shows that the electrode bias has little effect on the coherency, while the 0.24 T case shows it to be increased by 14% over the nonbiased case. These observations of increasing fluctuation levels within the strong poloidal flows are in contrast to the theory⁸ and other experimental evidence,²³ indicating that a sheared poloidal rotation quenches the plasma turbulence, thus reducing the density and potential fluctuation amplitudes.

Another component in the calculation of the fluctuation-induced transport is the relative phase angle between the plasma density and potential oscillations, represented by $\alpha_{n\phi}(\omega)$ in Eq. (2). Profiles of the $\sin[\alpha_{n\phi}(\omega)]$ shown in Figs. 15(b) and 16(b) do show a significant difference between biased and unbiased conditions. Here, $\sin[\alpha_{n\phi}(\omega)]$ in the biased case is predominantly negative for both magnetic fields, and may account for some of the sign reversal in the observed transport. The influence of the poloidal rotation is such to shift the density and potential fluctuation phase relationship, so as to make $\sin[\alpha_{n\phi}(\omega)]$ negative. This appears to be the mechanism for changing

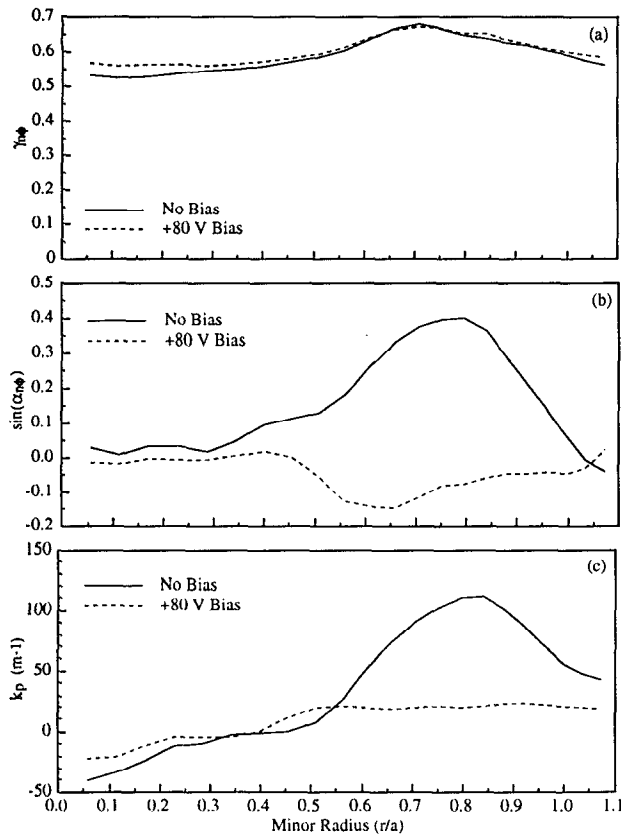


FIG. 16. Radial profiles of (a) average coherence, (b) phase angle relationship, and (c) $k_p(\omega)$, for plasma density and potential fluctuations, showing the effects of electrode biasing at a 0.26 T magnetic field operation.

the fluctuation-induced transport in IMS biased discharges.

The radial profiles of the final component in Eq. (2), $k_p(\omega)$, is presented in Figs. 15(c) and 16(c). Along with $\sin[\alpha_{n\phi}(\omega)]$, $k_p(\omega)$ can have negative values, which can make the overall integrated fluctuation-induced transport negative. However, for the 0.24 T case, Fig. 15(c) shows that the average value of $k_p(\omega)$ is positive for both the nonbiased and biased electrode configurations. For the 0.26 T field, Fig. 16(c) shows $k_p(\omega)$ to have both positive and negative values, but in the region where the overall transport is negative ($r/a > 0.5$), $k_p(\omega)$ is, again, positive for the biased and unbiased conditions. Thus, this analysis indicates that the predominantly negative fluctuation-induced transport seen for both magnetic field strengths results from the phase relationship of the density and potential fluctuations. When there is no induced poloidal rotation, the value of $\sin[\alpha_{n\phi}(\omega)]$ indicates that the phase of the potential fluctuations lead those of the density fluctuations. However, when there is a strong poloidal flow, this phase relationship is reversed to produce the negative fluctuation-induced transport.

D. Reynolds stress and poloidal flows

The computed Reynolds stress-driven flow, Eq. (3), for unbiased IMS discharges is presented in Fig. 17 for

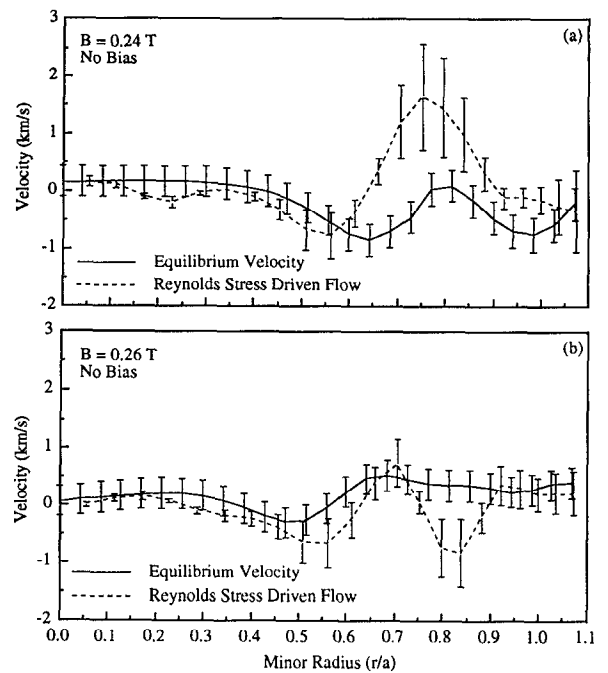


FIG. 17. Comparison of Reynolds stress-driven poloidal flows and equilibrium poloidal flow velocity for (a) 0.24 T magnetic field and (b) a 0.26 T magnetic field.

each magnetic field strength. Also shown for comparison [shown previously in Figs. 13(b) and 14(b)] is the equilibrium poloidal flow velocity computed from the measured density, ion pressure, and potential profiles through momentum balance, Eq. (4). Here, we see that flows can be induced as a result of the Reynolds stress term using measured plasma parameters, and that these flows are comparable in magnitude to that of the equilibrium velocity for unbiased IMS discharges. This flow is not significant in the biased electrode configurations, since the induced electric field dominates the poloidal flow drive.

For unbiased IMS plasmas, the pressure gradient-driven flow velocity term ($\nabla P/enB$) is comparable in magnitude, and directed opposite to the $\mathbf{E} \times \mathbf{B}$ driven flow term ($-E/B$). In an equilibrium condition with no poloidal flow, these terms would exactly cancel each other over the entire minor radius. Thus, where these terms do not cancel each other indicates a possible external mechanism inducing a nonzero poloidal flow.

The radial distribution of the Reynolds stress-driven flow does not quantitatively agree with the equilibrium flow for either field. Although the error bars are large, the equilibrium profile in the 0.24 T case [Fig. 17(a)] shows some significant deviations from zero poloidal flow, which indicates that there might be some external mechanism driving a poloidal flow. The profile in the 0.26 T case does not show significant deviations from zero flow, and suggests this configuration has no flow drive. In either case, the flow is small, and an independent measure of the poloidal flow is not available to confirm the existence of the Reynolds stress-driven flows.

IV. SUMMARY

A two-dimensional description of the electrostatic fluctuation-induced particle transport has been obtained for the IMS stellarator using Langmuir and emissive probes. In addition, these measurements show the steady-state values, as well as the fluctuation characteristics of the plasma density, electron temperature, and plasma potential in the entire poloidal cross section for comparison with the measured fluctuation-induced transport. The measurements were performed at two values of central magnetic field strength, which exhibits a large difference in particle confinement time to determine what role the fluctuations may play in the particle confinement. Also, a positively biased electrode positioned just inside the separatrix is used to induce a large poloidal plasma rotation to study the impact of this rotation on the fluctuations and the resulting particle flux.

The measurements show that transport due to electrostatic fluctuations is the major loss mechanism for the magnetic field configuration where a low particle confinement time is observed. Fluctuation-induced transport accounts for 87% of the total particle losses in the device when the field strength places the ECH resonance on the axis of IMS (0.26 T on axis), as opposed to only 10% of the total particle losses when the ECH resonance is placed on the inside, or high-field side of the torus (0.24 T on axis). Since there is only a 7% change in magnetic field strength between these configurations, the resulting change in particle confinement time is attributed to be the interaction of the ECH resonance location with the equilibrium plasma that produces the high level of fluctuation-induced transport. Previous studies have shown that the remaining particle transport may be due to convection in these unbiased IMS discharges.²⁴ The potential contours do not line up as well with the magnetic flux surfaces in the nominal (no electrode bias) discharges, as when the electrode is biased.

The impact of the induced poloidal rotation by the electrode bias is to make the radial fluctuation-induced transport negative, or inward. Examination of the components used to calculate the fluctuation-induced flux shows the negative transport is due to a relative phase shift of the density and potential fluctuations. The standard case (no poloidal rotation) shows that the phase of the potential fluctuations leads the phase of the density fluctuations and produces positive transport, while the biased case (strong poloidal rotation) shows the phase of the density now leads that of the potential fluctuations, which results in negative particle transport.

The density, electron temperature, and potential fluctuation amplitudes are not generally diminished by the induced sheared poloidal flow caused by the biased electrode. This result contradicts the observations in Texas Experimental Tokamak²³ (TEXT), where a correspondence was found between lower fluctuation levels in regions of high poloidal velocity shear. These fluctuation levels also show a significant increase with the minor radius corresponding to the position, where the gradient in pressure leads to unfavorable curvature.

The two-dimensional fluctuation-induced transport distribution is poloidally asymmetric in the standard configurations, and remains asymmetric in the region of induced sheared poloidal rotation. The assumption of poloidally uniform fluctuation-induced particle transport cannot be made in IMS.

Finally, the Reynolds stress-drive flows are computed from the measured fluctuating radial and poloidal velocities. These flows are comparable in magnitude to the equilibrium plasma flow, and show some qualitative agreement with the radial profile of the equilibrium flow for the nominal IMS discharges (no electrode bias). However, the accuracy of the Reynolds stress flow estimations, and the lack of an independent measurement of the steady-state poloidal flow, make the determination of the existence of a Reynolds stress turbulent-driven poloidal flow difficult to confirm.

ACKNOWLEDGMENT

This work was supported by the U. S. Department of Energy, under Contract No. DE-FG02-86ER-53216.

- ¹P. C. Liewer, Nucl. Fusion **25**, 543 (1985).
- ²A. J. Wootton, B. A. Carreras, H. Matsumoto, K. McGuire, W. A. Peebles, Ch. P. Ritz, P. W. Terry, and S. J. Zweben, Phys. Fluids **B 2**, 2879 (1990).
- ³S. J. Levinson, J. M. Beall, E. J. Powers, and R. D. Bengtson, Nucl. Fusion **24**, 527 (1984).
- ⁴P. C. Liewer, J. M. McChesney, S. J. Zweben, and R. W. Gould, Phys. Fluids **29**, 309 (1986).
- ⁵W. L. Rowan, C. C. Klepper, Ch. P. Ritz, R. D. Bengtson, K. W. Gentle, P. E. Phillips, T. L. Rhodes, B. Richards, and A. J. Wootton, Nucl. Fusion **27**, 1105 (1987).
- ⁶T. Uckan, C. Hidalgo, J. D. Bell, J. H. Harris, J. L. Dunlap, J. B. Wilgen, Ch. P. Ritz, T. L. Rhodes, and A. J. Wootton, J. Nucl. Mater. **176-177**, 693 (1990).
- ⁷T. D. Rempel, C. W. Spragins, S. C. Prager, S. Assadi, D. J. Den Hartog, and S. Hokin, Phys. Rev. Lett. **67**, 1438 (1991).
- ⁸H. Biglari, P. H. Diamond, and P. W. Terry, Phys. Fluids **B 2**, 1 (1989).
- ⁹D. T. Anderson, J. A. Derr, and J. L. Shohet, IEEE Trans. Plasma Sci. **PS-9**, 212 (1981).
- ¹⁰R. R. Weynants, R. J. Taylor, P. E. Vandenplas, F. Durodie, B. Schweer, D. Bora, T. Delvigne, J. Devos, K. H. Dippel, M. Gaigneaux, B. Giesen, Y. T. Lie, A. M. Messiaen, R. Moyer, U. Samm, R. P. Schorn, C. Stickelmann, R. Van Nieuwenhove, G. Van Oost, G. H. Wolf, and J. W. Yang, in *Proceedings of the 17th EPS Conference on Controlled Fusion and Plasma Heating*, Amsterdam, 1990 (European Physical Society, Petit-Lancy, Switzerland, 1990), Vol. 1, p. 287.
- ¹¹R. J. Taylor, M. L. Brown, B. D. Fried, H. Grote, J. R. Liberati, G. J. Morales, P. Pribyl, D. Darrow, and M. Ono, Phys. Rev. Lett. **63**, 2365 (1989).
- ¹²P. H. Diamond and Y. B. Kim, Phys. Fluids **B 3**, 1626 (1991).
- ¹³R. P. Doerner, Ph.D. thesis, University of Wisconsin-Madison, Department of Electrical and Computer Engineering, 1988.
- ¹⁴N. Hershkowitz, in *Plasma Diagnostics*, edited by O. Auciello and D. L. Flamm (Academic, San Diego, CA, 1989), Vol. 1.
- ¹⁵S. S. Medley and D. R. A. Webb, J. Phys. D Appl. Phys. **4**, 658 (1971).
- ¹⁶E. Leal-Quiros and M. A. Prelas, IEEE Trans. Plasma Sci. **PS-16**, 661 (1988).
- ¹⁷F. F. Chen, in *Plasma Diagnostic Techniques*, edited by R. H. Huddleston and S. L. Leonard (Academic, New York, 1965).
- ¹⁸E. J. Powers, Nucl. Fusion **14**, 749 (1974).
- ¹⁹B. J. Peterson, D. T. Anderson, F. S. B. Anderson, M. Coronado, J. L. Shohet, and J. N. Talmadge, Bull. Am. Phys. Soc. **37**, 1548 (1992).
- ²⁰M. Coronado and J. N. Talmadge, Phys. Fluids **B 5**, 1200 (1993).

- ²¹F. S. B. Anderson, B. J. Peterson, D. T. Anderson, and J. L. Shohet, *Bull. Am. Phys. Soc.* **35**, 2031 (1990).
- ²²Ch. P. Ritz, R. V. Bravenec, P. M. Schoch, R. D. Bengtson, J. A. Boedo, J. C. Forster, K. W. Gentle, Y. He, R. L. Hickok, Y. J. Kim, H. Lin, P. E. Phillips, T. L. Rhodes, W. L. Rowan, P. M. Valanju, and A. J. Wootton, *Phys. Rev. Lett.* **62**, 1844 (1989).
- ²³Ch. P. Ritz, H. Lin, T. L. Rhodes, and A. J. Wootton, *Phys. Rev. Lett.* **65**, 2543 (1990).
- ²⁴J. N. Talmadge, C. A. Storlie, D. T. Anderson, F. S. B. Anderson, R. P. Doerner, P. H. Probert, J. L. Shohet, and P. K. Trost, *Nucl. Fusion* **29**, 1806 (1989).